Chapter 3

Isomeric Coformer Responsive Conformational Adjustment to Recuperate Stability, Solubility, and In Vitro Permeation Behavior of Drug Molecular Salts

3.1 Abstract

The N–H or O–H systems are highly electron-deprived, and hence they easily interact with lone pairs usually on other N or O atoms in an extra bonding interaction. Such steering interactions stimulate the drug conformation to reposition that mounts well with all interactions and the packing in the lattice. Conformationally flexible histamine H_2-receptor inhibitor drug famotidine (FAM) that shows low bioavailability and rapid degradation in an acidic environment was picked from the laboratory shelves. Six molecular salts of FAM with coformers of isomeric aminobenzoic acids (ABA) and isomeric hydroxybenzoic acids (HBA) from the GRAS list were synthesized via mechanochemical grinding. The obtained multicomponent solids show enhanced phase stability when compared to the parent drug in three different pH media. The molecular salts with *o*-HBA, *o*-ABA, and *p*-ABA show comparable solubility at pH 1.2, whereas the rest exhibited superior solubility and membrane permeation behavior in simulated physiological pH environments. This improvement of the drug properties is attributed to (i) the formation of directional hydrogen bond heterosynthons between the drug and coformers and the (ii) solute···solvent interactions. The change in the functional group(s), i.e., OH to NH_2, and the isomeric position variation aided in altering the conformation of the drug molecules leading to unique crystal packing in the solid states and corroborating with improved properties.

3.2 Introduction

The synthesis of cocrystal and/or salt relies on the intermolecular interactions, explicitly the directional hydrogen bonds between solute···solute and solute···solvent [1–4]. Thus, the rational multicomponent crystal design with desirable properties is centered on the expected supramolecular interactions [3–6]. Stability, solubility, and membrane permeation are a few fundamental prerequisites in the development of a drug to achieve maximum efficacy [7]. The molecular salt formulation is a proven technology to modify drug pharmacokinetic properties, and over 50% of drug compounds in the market are administered in salt formulations treasured today [8–13]. The only limitation is that it only

works for drug candidates with an ionizable functional group. Cocrystal formulation is in place as an alternative and effective method to tune the solid-state properties of drugs with no ionizable functional groups [14–19]. Famotidine (FAM), a class IV drug in the BCS classification, is used as an inhibitor of histamine H_2 receptors to treat peptic ulcers, gastroesophageal reflux, etc.[20,21]. The drug exhibits very low and variable oral bioavailability that ranges from 20 to 66% depending on conditions [22]. Apart from low solubility and poor permeability, the drug degrades in acidic conditions and its therapeutic activity is reduced [23]. It is worth mentioning that the drug has two polymorphic modifications, Form A and Form B, where metastable Form B is the marketed form that easily transforms to stable Form A during grinding [24].

The chemical stability, aqueous solubility, and oral bioavailability enhancement of the drug FAM have been studied by complex formation with carboxymethyl-β-cyclodextrin [25]. Optional methods such as solid dispersion were employed to improve the FAM solubility, dissolution rate, and in vivo effectiveness against gastric fluid hyperacidity [26]. Salt-forming agents such as salicylic acid can improve the drug solubility when compared to the parent drug, as demonstrated by Brittain [27]. Following up, FAM-maleate salt and cocrystal of FAM with malonic acid were further studied and found to be stable and better soluble than the pure drug [28,29]. Recently, the degradation behavior of FAM at simulated physiological pH conditions and synthesis of three cocrystals of FAM with xanthine derivatives that displayed superior phase stability in different pH environments was reported [20].

Table 3.1 Reported cocrystals/salts of FAM with improved physicochemical properties.

Coformers	Solid forms	Evaluated property	References
Salicylic acid	salt	solubility	[27]
Maleic acid	salt	stability and solubility	[28]
Malonic acid	cocrystal	solubility	[29]
Xanthine derivatives	cocrystals	stability	[20]

This chapter demonstrates the synthesis of six molecular salts of the drug FAM that show high stability and improved physicochemical properties, including solubility, membrane permeation, and drug flux. Isomeric monohydroxybenzoic acids and isomeric aminobenzoic acids are chosen from the acceptable molecules listed as salt/cocrystal former (Scheme 3.1). These coformers are selected to comprehend the variation in

properties driven by (i) the functional group's competition, phenolic –OH vs –NH_2, and (ii) the isomeric position variation, which can be a guide for the optimal salt formulation with faster dissolution and high permeability. The isomeric position change of functional groups in the coformer facilitated drug conformation change into a unique crystal packing behavior in the solid states that substantiates improved properties by the salt formulation.

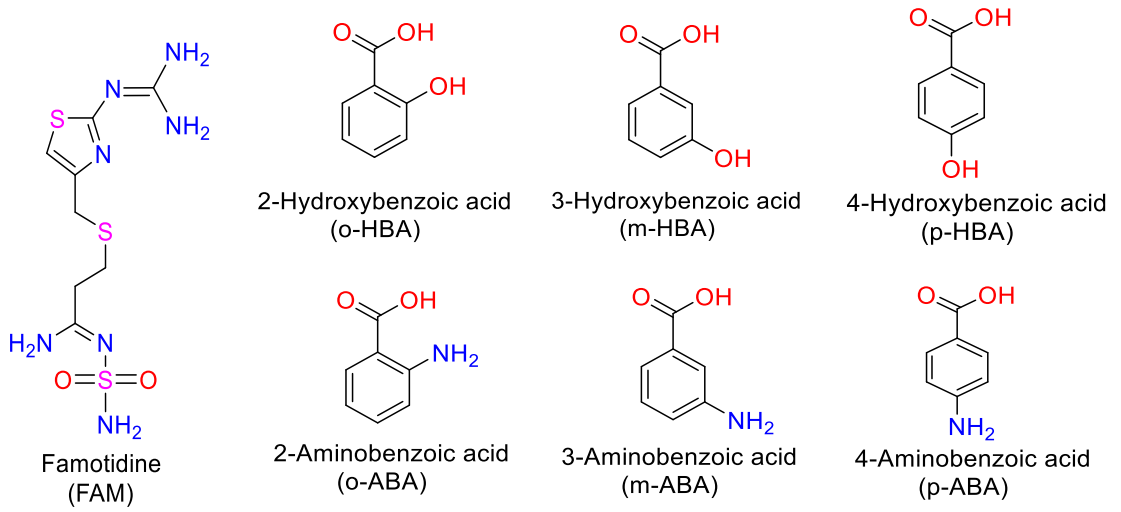

Scheme 3.1 Molecular structures of the drug famotidine and isomeric aminobenzoic acid and isomeric hydroxybenzoic acids as coformers.

3.3 Results and Discussion

3.3.1 Synthesis of Molecular Salts

Famotidine is a weak base (pK_a = 6.8 at guanidine N) and has amino, imine, thiazole, and sulfonamide functional groups that are ionizable at different pH conditions. It undergoes protonation at the N of guanidine and amidine moieties at low pH [30]. It is expected to form strong hydrogen bonds with acidic coformers through the formation of neutral guanidine···acid (i.e., a cocrystal) or ionic guanidinium···carboxylate (i.e., molecular salt) supramolecular heterosynthons [28,29]. The two sets of coformers displayed in Scheme 3.1 resulted in six molecular salts in a 1:1 ratio (C-1 to C-6). All structures were isolated as monohydrate structures (Table 3.2). They were characterized and subjected to aqueous solubility, membrane permeability, and phase stability determination. Single crystal X-RD analysis supports the occurrence of anticipated hydrogen bond-based ureide···ureide and guanidine···ureide synthons. These supramolecular synthons are responsible for the self-assembly of the primary structural motif extended into three-dimensional (3D) molecular packing in their crystalline lattice.

Table 3.2 Cocrystallization of FAM with isomeric hydroxybenzoic acids and aminobenzoic acids resulted in hydrated molecular salts, C-1 to C-6.

API	coformers	molecular salts	Stoichiometric ratio
Famotidine (FAM)	2-Hydroxybenzoic acid	C-1 [FAM:*o*-HBA:H_2O]	1:1:1
	3-Hydroxybenzoic acid	C-2 [FAM:*m*-HBA:H_2O]	1:1:1
	4-Hydroxybenzoic acid	C-3 [FAM:*p*-HBA:H_2O]	1:1:1
	2-Aminobenzoic acid	C-4 [FAM:*o*-ABA:H_2O]	1:1:1
	3-Aminobenzoic acid	C-5 [FAM:*m*-ABA:H_2O]	1:1:1
	4-Aminobenzoic acid	C-6 [FAM:*p*-ABA:H_2O]	1:1:1

3.3.2 Characterization of Product Phases

Vibrational Spectroscopy (FT-IR). The FT-IR absorption spectra of C-1 to C-6 are presented in Figure 3.1 with a comparison of FT-IR stretching frequencies with that of pure FAM. Significant variation in the IR spectra checks for the ionic guanidinium···carboxylate heterosynthons formation in the products. Observed IR frequencies are listed in the experimental section 3.5.3. The change in IR frequencies reveals the formation of new intermolecular hydrogen bonds, O–H···N and N–H···O between the coformer and drug. Sharp IR absorption peaks at the carboxylate anion absorption region suggest a transfer of the proton from the most acidic COOH hydrogen to the basic N center of FAM. Besides, the ΔpK_a rule of three also supports predicting the formation of molecular salts of FAM with both series of coformers [31–34]. The ΔpK_a values fall in the uncertain range of salt or cocrystal formation (Table 3.3). Therefore, either a complete transfer of proton or a salt−cocrystal continuum formation was anticipated in the products. The crystal structure analysis part, discussed in the following section, resolves the location of the proton. The COOH proton is fairly positioned near the N-atom on the guanidine moiety of FAM but with a variable distance from the –COOH oxygen (Figure 3.2). Such a salt-cocrystal continuum or the proton transfer behavior [whether it is in an ionic ($O^{-}\cdots H–N^{+}$) state or a neutral adduct (O–H···N)] can easily be assessed by X-ray photoelectron spectroscopy (XPS) [35].

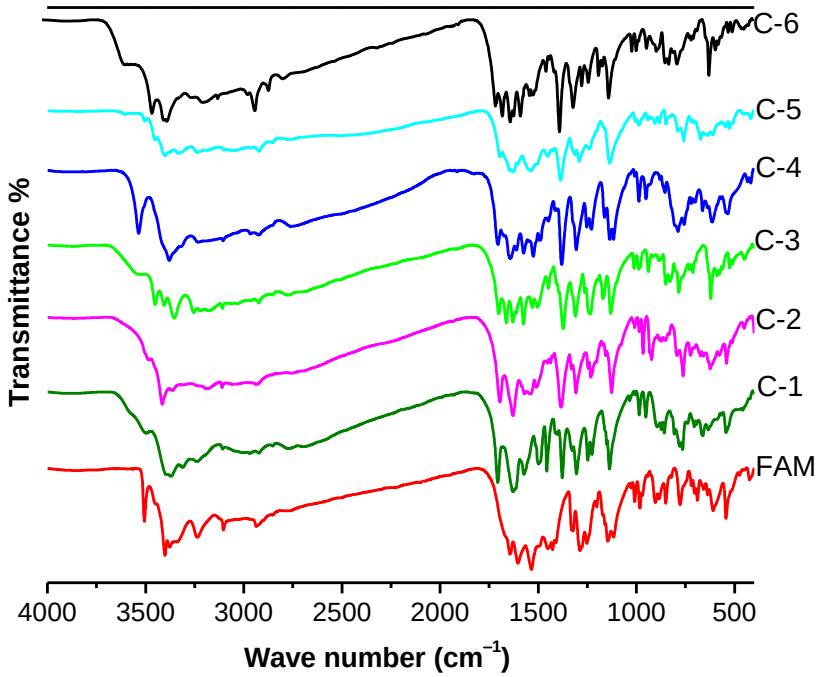

Figure 3.1 Vibrational absorption frequencies of various functional groups in molecular salts C-1 to C-6, compared with that of the pure drug FAM.

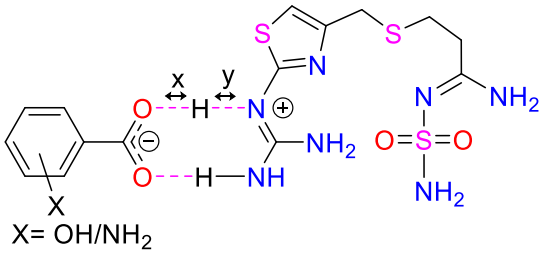

Figure 3.2 Guanidinium···carboxylate hydrogen bond heterosynthon in FAM salts.

Table 3.3 The ΔpK_a values of FAM and coformers. The COOH hydrogen atom location was estimated from single crystal X-ray data analysis to understand the proton transfer phenomenon in the products (Figure 3.2).

API (pK_a)	coformer (pK_a)	acid-base ΔpK_a	product	distance (Å)		angle (°)	solid form
				x	*y*		
FAM (6.8)	*o*-HBA (2.79)	4.01	C-1	2.00	0.77	175	salt
	m-HBA (3.84)	2.96	C-2	1.93	0.88	164	salt
	p-HBA (4.38)	2.42	C-3	2.01	0.78	170	salt
	o-ABA (4.89)	1.91	C-4	1.83	0.88	175	salt
	m-ABA (4.81)	1.99	C-5	1.79	0.89	173	salt
	p-ABA (4.77)	2.03	C-6	1.89	0.88	171	salt

Differential Scanning Calorimetry (DSC). The melting onset temperatures for C-1 to C-6 were recorded using a DSC instrument, and values are presented in Table 3.4. The melting onsets of the products are different from those of their respective starting materials. The water loss endotherms in the DSC plots either overlapped with the melting temperature of the product or underwent dehydration during sample preparation time. Broad DSC endothermic transitions observed at < 120 °C indicate the presence of water molecules of crystallization (Figure 3.3).

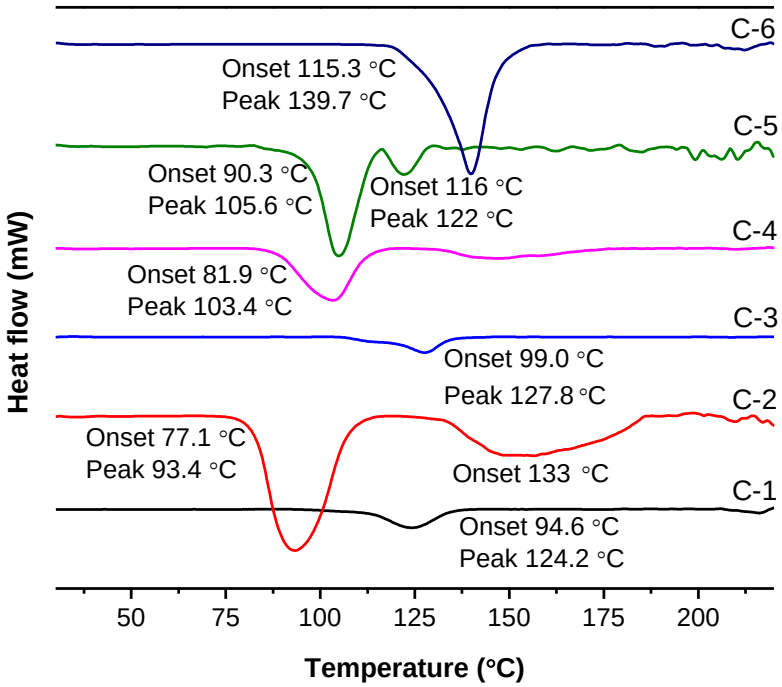

Figure 3.3 DSC endotherms represent the melting onset of the six molecular salts of FAM.

Table 3.4 DSC endotherms represent the melting onset and peak of the salt hydrates**.**

API (M. Pt.)	coformers	coformer M. Pt. (°C)	salts	salts M. Pt. (°C)	
				onset	peak
FAM (161-164°C)	*o*-HBA	158.6	C-1	94.6	124.2
	m-HBA	202	C-2	77.1	93.4
	p-HBA	214.5	C-3	99.0	127.8
	o-ABA	146-148	C-4	81.9	103.4
	m-ABA	178-180	C-5	90.4	105.6
	p-ABA	187	C-6	115.3	139.7

Thermogravimetric Analysis (TGA). The TGA plots further imply the presence of water molecules in these structures. The thermogravimetric weight loss for C-1 is observed as 3.40% below 120 °C (Calcd 3.65%). Similarly, weight loss is observed as 3.53 and 3.50% for C-2 (Calcd 3.65%) and C-3 (Calcd 3.65%) respectively (Figure 3.4). The respective weight loss percentages suggest a monohydrate structure. Similarly, monohydrate formation for C-4 (obs. 3.42%), C-5 (obs. 3.63%), and C-6 (obs. 3.52%) is also estimated by TGA and further confirmed by the single crystal X-ray analysis discussed in subsequent sections.

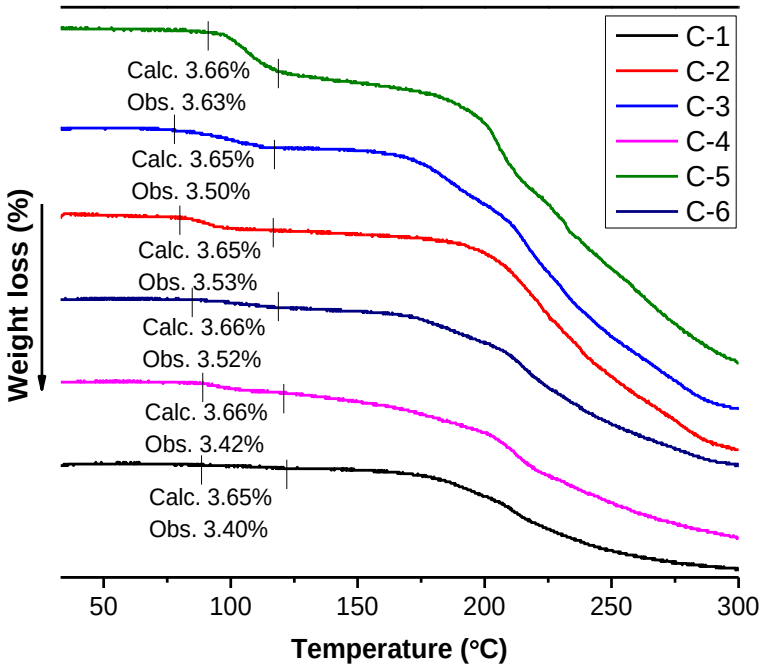

Figure 3.4 Weight loss measured by TGA agrees well with a 1(Drug):1(Coformer):1(Water) ratio molecular salt confirmed by single crystal X-ray structure elucidation.

Powder X-ray Diffraction (PXRD). The experimental PXRD patterns of all six molecular salts are unique (Figure 3.5) and different from their respective starting materials. The phase purity of each material was tested with the experimental PXRD pattern, which was compared by Rietveld refinement with the simulated pattern extracted from the corresponding single crystal structure. The Rietveld refinement was performed using Powder Cell 2.3, and overlaid plots are available in Appendix Figure A2. The overlaid PXRD patterns show identical intensity patterns and peak positions, confirming the crystalline phase purity and homogeneity of all products.

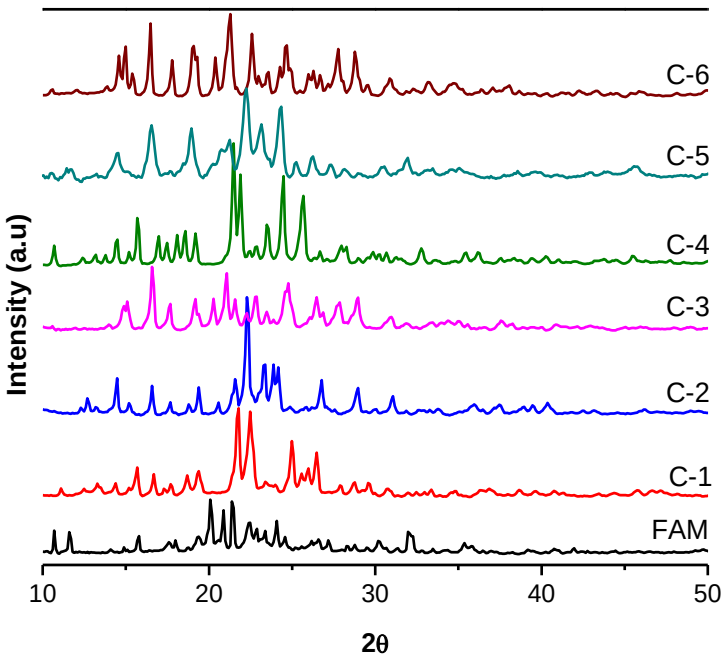

Figure 3.5 PXRD patterns of the six FAM molecular salts, *viz* C-1 to C-6.

Single Crystal X-RD. Single crystal X-ray structures were determined to understand the molecular packing and intermolecular interactions that control the solid-state properties. Crystals were obtained using neat or solvent drop grinding followed by slow evaporation from methanol. The formation of guanidinium···COO^- hydrogen bond synthon is observed in all crystal structures (Figure 3.2). The high ΔpK_a value between the guanidine and COOH group drives the proton of the COOH group to transfer to the guanidine N atom forming an ionic $R_2^2(8)$ heterosynthon. The water molecule joins these hydrogen-bonded heterosynthons to complete 3D molecular arrangements in the lattice. Crystal data parameters are tabulated in Appendix Table A2 and hydrogen bond geometries are displayed in Table 3.5. The crystal structure of C-1 is solved in an orthorhombic space group $P2_12_12_1$ with one symmetry-independent molecule of FAM, *o*-HBA, and H_2O. The expected $R_2^2(8)$ supramolecular heterosynthon between guanidine and COOH is formed through neutral N–H···O and ionic N^+–H···O^- hydrogen bond connections. The NH_2 group of the sulfonamide moiety is connected to a water molecule via an N–H···O hydrogen bond. The water OH is hydrogen-bonded to the OH group oxygen of *o*-HBA. The N–H···O hydrogen bond from the NH_2 group of imine moiety to OH of *o*-HBA forms a cyclic supramolecular ring motif (Figure 3.6a). Such aggregates are further connected through O–H···O hydrogen bonds, resulting in a two-dimensional (2D) sheetlike structure (Figure 3.6b).

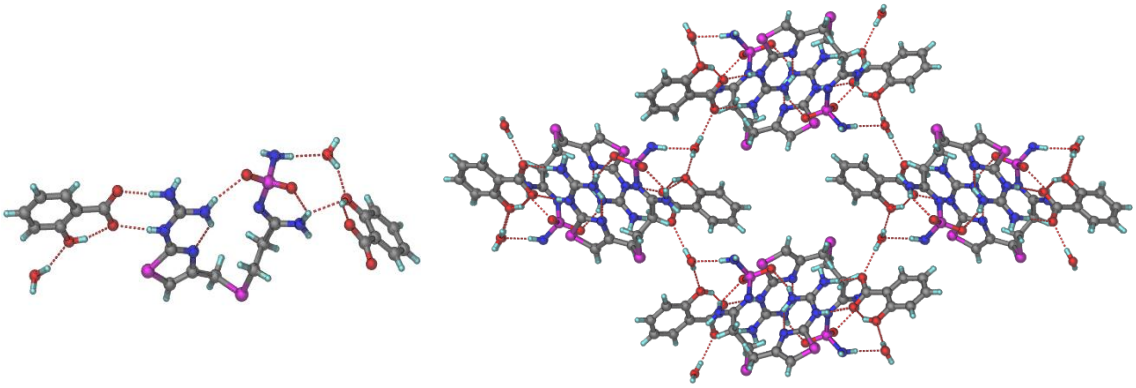

(a) (b)

Figure 3.6 (a) Ionic guanidinium···COO^- heterodimers in the **C-1** crystal structure. Water molecule connects such drug···conformer units via O–H···O hydrogen bonds supported by auxiliary N–H···O hydrogen bonds. (b) Water molecules further connect the aggregates of dimers via O–H···O hydrogen bonds.

Product C-2 crystallizes in the triclinic $P\bar{1}$ space group with one molecule of each FAM, *m*-HBA, and water. Two inversion symmetry-related water molecules form a dimer by O−H···O hydrogen bonds. Similarly, two inversely related FAM molecules form a dimer via $N–H_{(guanidine\ NH2)}$ ···$O_{(Sulfonamide\ S=O)}$ hydrogen bonds (Figure 3.7b). The water dimer connects four *m*-HBA molecules via O–H···O between OH to carboxylate ions and OH of *m*-HBA to water oxygen (Figure 3.7a). The O–H···O and N–H···O interactions are dominant in forming the extended 2D sheetlike structure along the crystallographic plane [100] (Figure 3.7b).

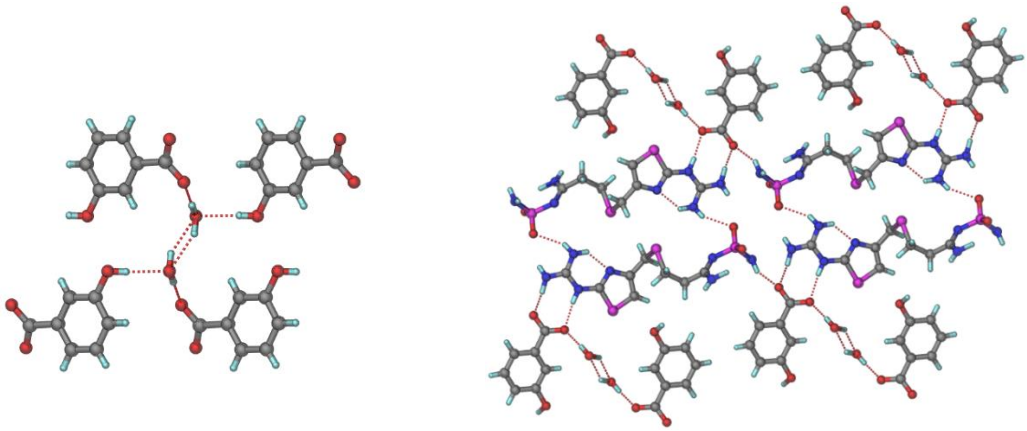

(a) (b)

Figure 3.7 (a) Dimeric water unit connects the $R_2^2(8)$ heterodimer that further extends to a tapelike structure via O–H···O and N–H···O hydrogen bonds. Such molecular tapes are linked through the OH group of the *m*-HBA coformer. (b) The $R_2^2(8)$ heterodimer between FAM and *m*-HBA is present in the C-2 crystal structure. Two inversion center-related FAM molecules form a dimer via $N–H_{(guanidine\ NH2)}$···$O_{(Sulfonamide\ S=O)}$ hydrogen bonds.

The guanidinium···COO^- hydrogen bond synthon confirms proton transfer. The crystal structure of C-3 is arranged in a monoclinic $P2_1/c$ space group with a 1:1:1 ratio of FAM, *p*-HBA, and water. The C-3 crystal structure exhibits similar molecular packing arrangements as it is found in C-1 and C-2 crystal structures. The water molecule connects the *p*-HBA molecules via O–H···O interactions into a one-dimensional molecular tape, which further expands through the $R_2^2(8)$ heterodimer between FAM and *p*-HBA, completing the 2D and 3D molecular packing in C-3 (Figure 3.8).

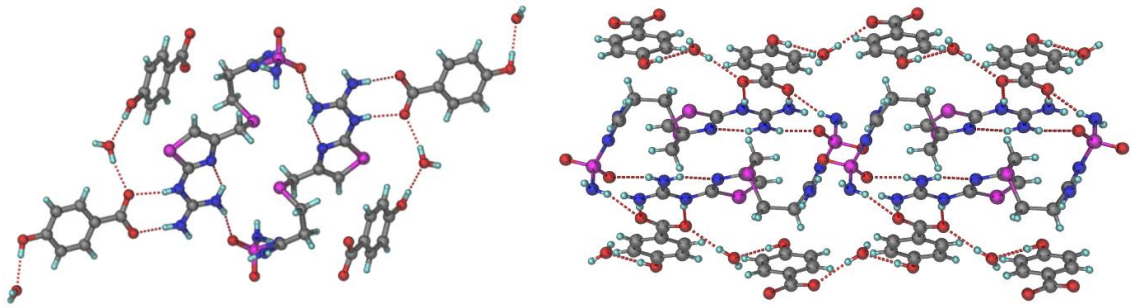

(a) (b)

Figure 3.8 (a) As observed in the crystal structures of C-1 and C-2, the $R_2^2(8)$ ring motif via N^+–H···O^- and N–H···O strong interactions are also formed in the C-3. Water molecule acts as a linker between these supramolecular dimers. (b) The layered crystal structure of C-3 is linked by the $R_2^2(8)$ ring motif along the crystallographic axis [100].

Crystal structures of FAM with isomeric aminobenzoic acids, i.e., C-4, C-5, and C-6, also exhibit analogous hydrogen bond patterns (Figures 3.9 and 10). The basic difference in their crystal structures is that the extended molecular packing is driven by N–H···N hydrogen bonds between NH_2 groups of *isomeric*-ABA and NH_2 groups of FAM. The $R_2^2(8)$ ring motif formed via N^+–H···O^- and N–H···O strong interactions is associated by water molecules via N–H···O and O–H···O hydrogen bonds (Figure 3.9a). The N–H···N hydrogen bonds from NH_2 groups of imine moiety to NH_2 groups of *o*-ABA extend the molecular packing of C-4 in 2D (Figure 3.9b). The crystal structures of C-5 and C-6 reveal that the NH_2 group of the coformers does not take part in intermolecular interactions. In the C-5 structure, FAM molecules are involved in the formation of sulfonamide homodimers through $R_2^2(8)$ and $R_2^2(12)$ ring motifs via N–H···O hydrogen bonding. Besides the main $R_2^2(8)$ motif heterosynthon, each FAM molecule is further linked with the second *m*-ABA molecule via the $R_2^1(6)$ ring motif (Figure 3.10a,b). With the same composition with a 1:1:1 ratio of FAM, *p*-ABA, and water, the C-6 crystal structure is resolved in the monoclinic $P2_1/c$ space group. N–H···O hydrogen bonding from the NH_2

group of sulfonamide to the oxygen atom of the carboxylate of *p*-ABA molecule helps in connecting the $R_2^2(8)$ hydrogen-bonded dimer to form a layered structure of the C-6 (Figure 3.10d).

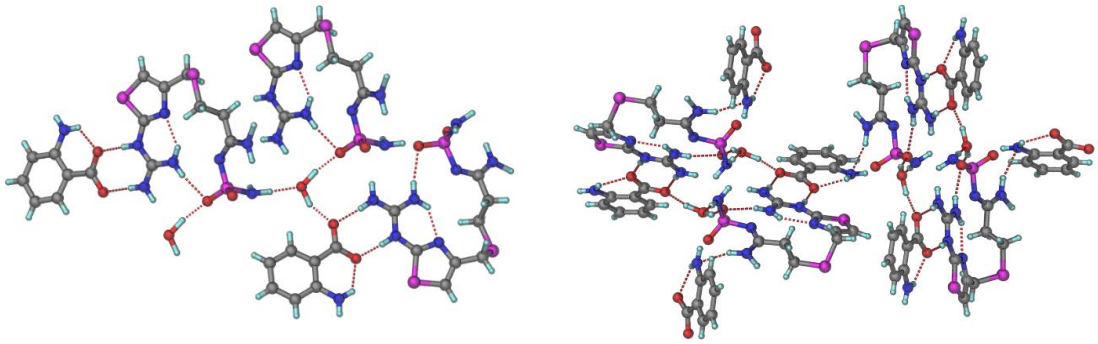

(a) (b)

Figure 3.9 (a) $R_2^2(8)$ heterosynthon between FAM and *o*-ABA formed via N^+–H···O^- and N–H···O strong interactions. Auxiliary N–H···O and O–H···O hydrogen bonds from water and the NH_2 group extend the molecular packing in the crystal lattice of C-4. (b) 3D molecular packing of C-4**.**

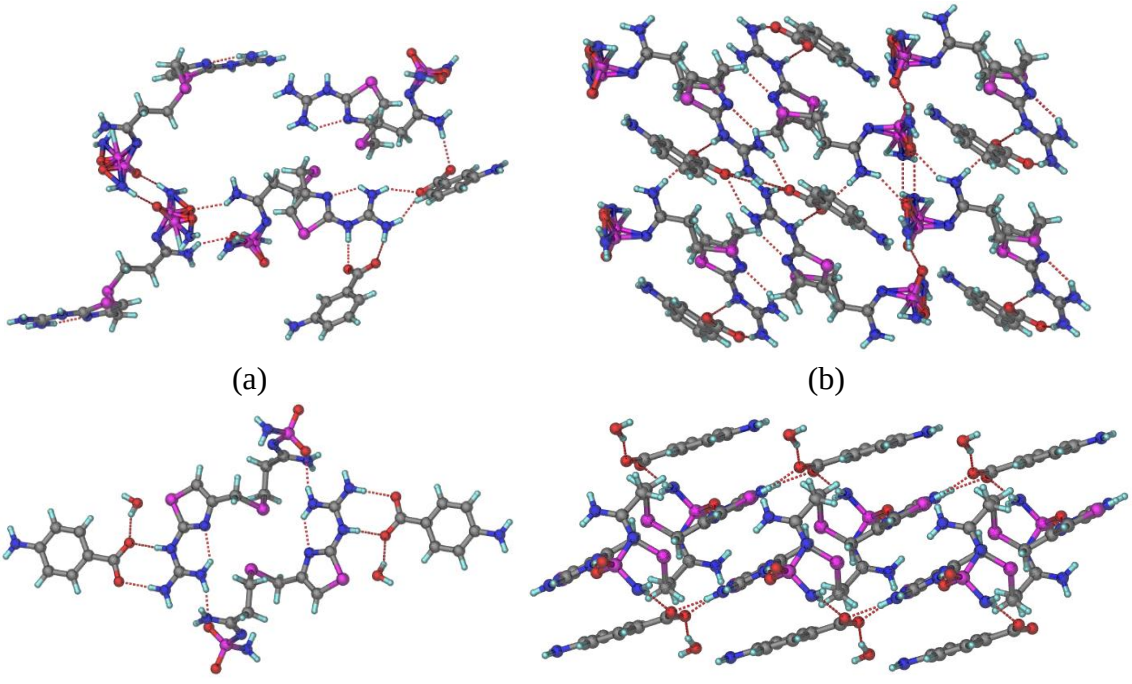

(a) (b)

(c) (d)

Figure 3.10 (a) Prime synthons in the crystal structure of C-5. (b) The sheetlike structure of C-5 is connected by N–H···O hydrogen bonds along the [10] plane. (c) *p*-ABA molecule is connected with FAM dimer by $R_2^2(8)$ ring motif in the crystal structure of C-6. (d) Crystal structure of C-6 is sustained by N–H···O hydrogen bonding to form a layer structure along the [001] axis.

Table 3.5 Important hydrogen bond parameters observed in the salts, C-1 to C-6.

salts	interaction	H···A (Å)	D···A (Å)	∠D−H···A (°)	symmetry code
C-1	N_1–H_1···O_3	1.77	2.806(4)	178	1 + x, y, z
	N_3–H_5···O_4	1.74	2.770(4)	174	1 + x, y, z
	O_6–H_{22}···O_3	1.91	2.893(5)	173	–x, 1/2 + y, 1/2 – z
	N_7–H_{16}···O_6	1.89	2.922(5)	173	–1/2 – x, 1– y, 1/2 + z
	O_6–H_{23}···O_5	1.97	2.914(5)	161	
C-2	N_1–H_{1B}···O_3	1.78	2.773(5)	158	– x, – y, 1 – z
	N_3–H_{3A}···O_4	1.78	2.785(4)	163	– x, – y, 1 – z
	O_5–H_{5E}···O_6	1.86	2.831(4)	170	1 + x, y, z
	N_5–H_{5C}···O_6	2.06	3.049(5)	158	
	O_6–H_{6C}···O_4	1.67	2.652(4)	176	
C-3	N_1–H_{1A}···O_3	1.75	2.777(3)	170	–1 + x, y, – 1 + z
	N_3–H_{3A}···O_4	1.76	2.784(3)	168	–1 + x, y, – 1 + z
	O_6–H_{6D}···O_4	1.89	2.856(3)	169	–1 + x, 1/2 – y, –1/2 + z
	N_7–H_{7D}···O_3	1.95	2.945(3)	160	2 – x, 1 – y, 1 – z
	N_5–H_{5D}···O_5	2.07	3.097(3)	173	1 + x, 1/2 – y, –1/2 + z
C-4	N_3–H_{3A}···O_3	1.67	2.700(9)	174	–1/2 – x, 1 – y, –1/2 + z
	N_1–H_{1A}···O_4	1.75	2.775(8)	170	–1/2 – x, 1 – y, –1/2 + z
	O_5–H_{5E}···O_1	1.85	2.797(8)	160	x, y, −1 + z
	N_7–H_{7D}···O_5	1.94	2.970(10)	170	1 + x, y, 1 + z
C-5	N_3–H_{3A}···O_3	1.65	2.678(2)	173	1 – x, – y, 1 – z
	N_1–H_{1B}···O_4	1.87	2.850(2)	157	1 – x, – y, 1 – z
	N_2–H_{2A}···O_4	1.94	2.848(2)	145	–1/2 + x, 1/2 – y, 1/2 + z
	N_8–H_{8A}···O_1	2.10	3.130(4)	174	x, 1 + y, z
C-6	N_3–H_{3A}···O_3	1.74	2.761(4)	170	1 + x, y, z
	N_1–H_{1A}···O_4	1.76	2.790(4)	174	1 + x, y, z
	O_5–H_{5F}···O_3	1.94	2.878(5)	158	x, 1/2 – y, 1/2 + z
	N_5–H_{5C}···N_8	2.11	3.115(4)	162	–1 + x, 1/2 – y, –1/2 + z
	N_7–H_{7C}···N_6	2.08	3.115(5)	176	1– x, 1– y, –z

Water inclusion in all of the crystalline solids is apparent as there is a mismatch of hydrogen bond donors and acceptors in C-1 to C-6. To compensate for such incongruity inclusion of H_2O into the crystal lattice is the first choice as it readily (i) forms hydrogen bonds with donors and/or acceptors and (ii) fits into the tiny voids allowed by the starting molecules. The major driving force in the structural difference is developed due to the difference in the functional groups, i.e., OH vs NH_2. The isomeric position of these two functional groups added an essential role in the packing of the molecules in the lattice. The auxiliary N–H···O and/or O–H···O hydrogen bonds due to the change in a functional group or the isomeric position lead to significant conformational variation in the drug FAM. An overlay of FAM conformations in the crystal structures of C-1 to C-6 is drawn using Mercury 4.1 coupled with Cambridge Structural Data (CSD) (Figure 3.11). The change in torsion angles is listed in Appendix Table A3. An analogous deviation of the torsion angle is detected independently in the molecular salts for *ortho*-, *meta*- and *para*-substituted

coformers (Figure 3.12). Such change in conformational deviation is irrespective of the functional group attached to it, viz., –OH and $–NH_2$ and have a significant impact on tuning the physicochemical properties of the drugs.

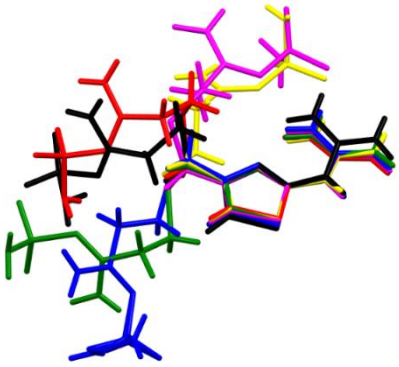

Figure 3.11 Overlay of FAM conformations extracted from the crystal structures of C-1 to C-6. [C-1 (yellow), C-2 (green), C-3 (red), C-4 (magenta), C-5 (blue), and C-6 (black)].

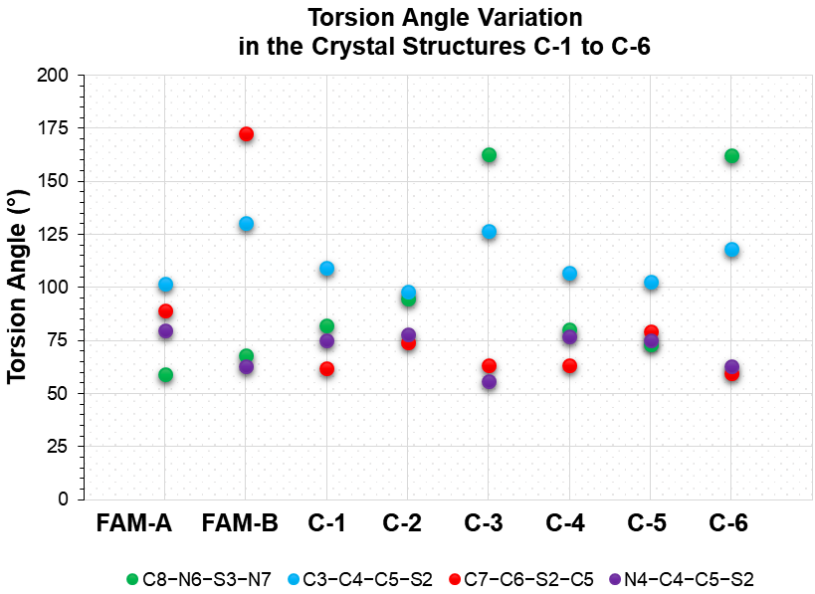

Figure 3.12 Conformational variation in FAM molecule was observed in the crystal structures of C-1 to C-6 through four different torsion angles referred to in Table A3.

3.3.3 Hydrogen Bond Synthon and CSD survey

The occurrence probability of hydrogen bond synthons in the molecular salts was assessed from the Cambridge Structural Database (CSD). A survey was performed by extracting the multicomponent organic molecular compounds having the functional groups (i) guanidine, (ii) sulfonamide, (iii) –COOH, and (iv) –OH, and v) $–NH_2$, which have no disorder, and the *R* factor is less than 10%. The analysis was done using CSD version 5.43, March 2022 update. The search for sulfonamide···acid heterosynthon results in 50 hits of which only one structure has guanidine, alcohol, and amine groups, whereas

guanidine···acid heterosynthon appeared in 39 crystal structures of which 13 (33.3%) contain alcohol group and 9 (23%) containing an amine group (Appendix Table A4). Except for XUHYUW and ZOGCOP, all the structures are in ionic form because of proton transfer from –COOH to imine N of guanidine moiety. The two common supramolecular synthons between guanidine and –COOH groups are shown in Figure 3.13. Out of 39 crystal structures, 26 structures have guanidine–carboxylic acid two-point synthon I (66.7%), and nine of them contain synthon II (23%). When an alcohol functional group is present in the structures, the probability of synthon I and II is reduced to approximately 20% and 5%, respectively. Similarly, in the presence of the amine group, their probability of formation is nearly 20% and 15%, respectively. In the reported structures, the occurrence of synthon II is found to be higher with the presence of the NH_2 group in the structure.

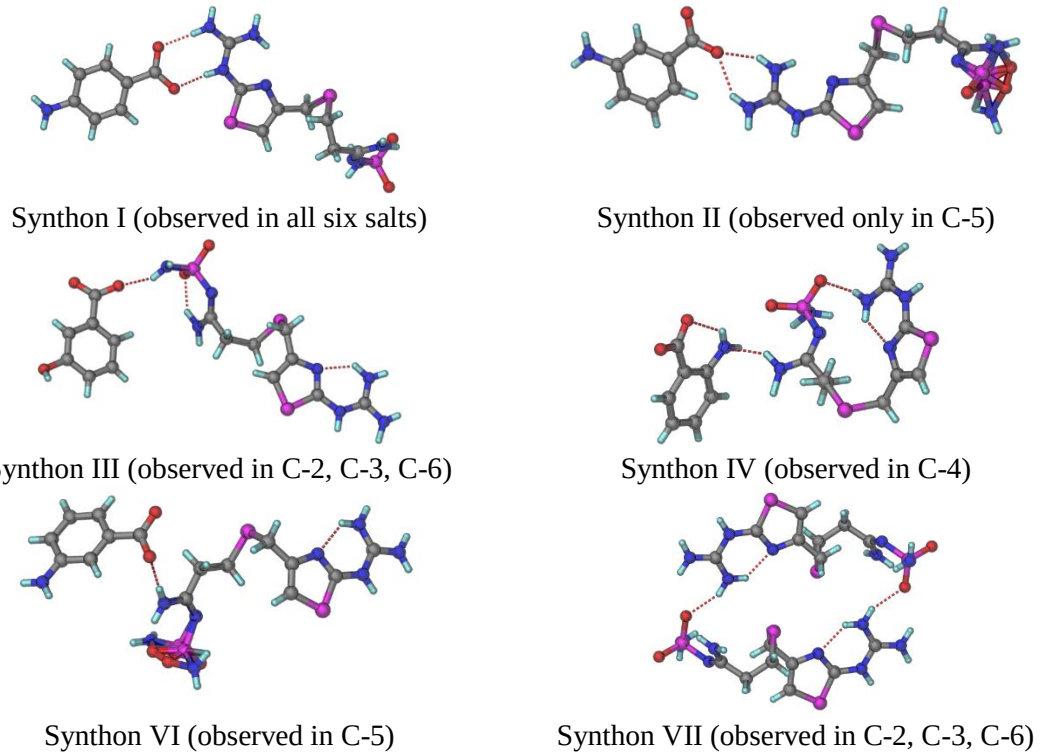

Figure 3.13 Observed hydrogen bond synthons in the crystal structures of C-1 to C-6 of the API and coformers. In all six products, synthon I is formed between guanidine and carboxylic acid as a prime synthon, while the others are formed as an auxiliary synthon in the presence of synthon I.

3.3.4 Phase stability study

The incorporation of a suitable coformer is to protect a sensitive drug's functional group, essentially improving the stability issues of the drug and its pharmacological properties.

The stability studies on drug compounds, such as caffeine, temozolomide, vitamin-D_3, nifedipine, etc., are a few noted examples that have improved drug stability through cocrystallization [36–39]. Phase stability tests were performed by preparing slurries in an aqueous medium and two common physiological pH environments. The PXRD patterns of samples from time to time were recorded to examine phase transformation if any occurring during the experiment (details in the Experimental Section 3.5.8). The PXRD pattern of the pure drug was compared with the patterns recorded for the material obtained from the slurry experiment within a time window of 24 h at (i) pH 1.2 and (ii) pH 7.4 and (iii) water (Figures 3.14 and A3, Appendix). The disappearance of a few observed peaks and a clear difference in peak positions for pure FAM at pH 1.2 indicate the stability issue of pure FAM and studied elsewhere [20]. At pH 1.2, the PXRD patterns recorded from time to time up to 24 h for all the salt products remain unchanged (Figures 3.14 and A3, Appendix). This indicates that the inclusion of coformer molecules in the crystal lattice of the drug FAM via strong hydrogen bonding such as N^+–H···O^-, N–H···O, and O–H···O provides better stability of the solid dosage form at pH 1.2.

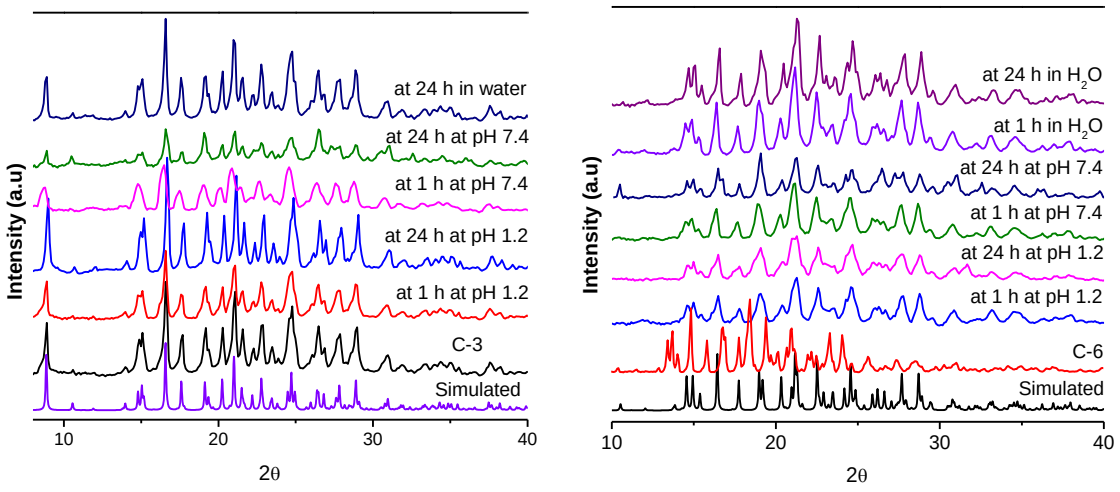

Figure 3.14 Phase stability study of C-3 (a) and C-6 (b) by a slurry experiment in an aqueous medium and buffer solution of pH 1.2 and 7.4. The constancy of PXRD patterns for C-3 and C-6 confirms their stability up to 24 h in all of the media. The stability study results of the other samples are presented in Appendix Figure A3.

A correlation with the single crystal structure reveals that the molecular conformation of the FAM is changed at different torsion angles due to the formation of the salts with the coformers (Figure 3.12 and Appendix Table A3). The torsion angle of the amidine moiety (C8–N6–S3–N7) in the crystal structure of the pure FAM (in Form A = 59.3° and Form B

= 67.9°) changes to 82.3° (C-1), 94.7° (C-2), 162.8° (C-3), 80.1° (C-4), 73.5° (C-5), and 162.3° (C-6). Such conformation change of the FAM molecules in the salt products leads to unique crystal packing in solid states, which may prevent the accessibility of the imine site in the amidine moiety. For instance, the dimeric motifs of two symmetry-related FAM molecules in C-3 and C-6 are connected to *p*-HBA and *p*-ABA via strong hydrogen bonding. Such dimer motifs are crammed between molecular layers formed from the coformer molecules. The molecular arrangement in the crystal lattice of C-3 and C-6 thereby protects the imine group on amidine moiety, which is sensitive to acid hydrolysis. Perhaps, the stability study in an aqueous medium and at pH 7.4 conditions confirms the stability of all product materials for up to 24 h or even longer periods (Figures A3, Appendix).

3.3.5 Solubility Measurement

Higher solubility of drugs can be achieved by incorporating highly soluble conformers in the crystal lattice of API [13]. The selected coformers in this study have higher aqueous solubility than API (Table 3.6), and therefore improved solubility is anticipated. The solubility of the drug FAM and C-1 to C-6 was measured in three different pH conditions (Figure 3.15). All six materials exhibit several-fold improvement in aqueous solubility compared to pure API: C-1 (6.11-fold), C-2 (23.5-fold), C-3 (17.81-fold), C-4 (6.66-fold), C-5 (18.15-fold), and C-6 (3.96-fold). At pH 1.2 condition, the solubility of C-2, C-3, and C-5 is 2 times, 1.27 times, and 1.4 times that of pure API respectively. But the solubility of C-1, C-4, and C-6 is slightly lower than that of pure API. At pH 1.2 condition, the solubility order of molecular salts of FAM with both isomeric HBA and ABA follows the same trend. Salts of *meta*-substituted coformers exhibited the highest solubility, followed by salts of *para*-substituted and *ortho*-substituted coformers. A similar solubility trend was also observed for the aqueous solubility of the salts, except salt of the *o*-ABA (C-4) exhibited better aqueous solubility than that of salt of *p*-ABA (C-6). At pH 7.4 condition, the solubility of the product materials is ~2 times that of the parent API. At this pH condition, only a minor variation in solubility was observed among the salt products despite changing the positions and/or types of function groups on the coformer. At pH 1.2 and in aqueous environments, when the OH group is at the *meta*- and *para*-positions, the multicomponent systems displayed better solubility as compared to the NH_2 group. For instance, the solubility of C-2 is 1.5 and 1.3 times that of C-5 at pH 1.2 and in pure water,

respectively, and the solubility of C-3 is 1.6 and 4.6 times of C-6 at pH 1.2 and in pure water, respectively. But the solubility of the salt of *o*-HBA (C-1) is slightly lower than that of salt of *o*-ABA (C-4). It can be seen from the plot that better solubility is observed at pH 1.2 in comparison to the other two media (Figure 3.15). The presence of the monovalent ions, i.e., Na^+ and Cl^- in the 1.2 pH medium and the ionic nature of salts (N^+–H···O^- interactions) facilitate the solute···solvent interactions. The reason behind the higher solubility observed for pure FAM at pH 1.2 is due to its ability to accept protons at low pH conditions by the basic N centers [30]. The protonated FAM can form a strong hydrogen bond with the polar solvent, which leads to enhanced solubility.

Table 3.6 The solubility comparison of starting materials with their respective salts.

sample	at pH 1.2 (28ºC)	at pH 7.4 (28ºC)	aqueous solubility (28ºC)	aqueous solubility of coformers
FAM	31.68	2.54	1.37	
C-1	18.77	4.46	8.37	2.24
C-2	64.74	4.39	32.21	7.25
C-3	40.07	5.68	24.8	5.0
C-4	20.38	4.53	9.13	5.7
C-5	44.01	4.69	24.87	5.9
C-6	25.06	6.5	5.42	4.7

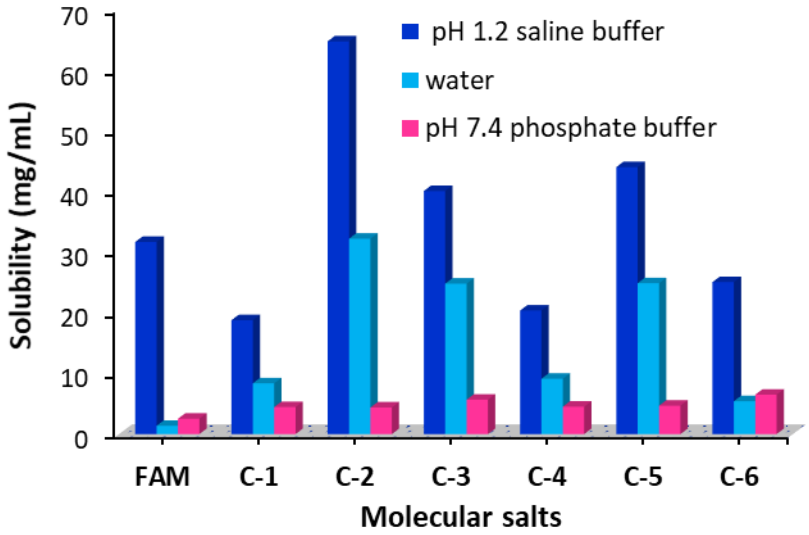

Figure 3.15 Solubility of pure FAM and its salts in pure water and at pH 1.2 and 7.4.

The solid-state properties of crystalline materials depend on the types and strength of intermolecular interactions, which determines the packing of molecules/ions in the crystalline materials. The crystal packing energy was computed to evaluate quantitatively the impact of various intermolecular interactions that are responsible for the observed

physicochemical properties. The packing energy of the products was calculated on Mercury 4.1 connected with CSD using Gavezzotti and Filippini force-fields. Marginal differences in packing energy were observed among the product materials (Figure 3.16). Solid materials with lower negative packing energy are thermodynamically less stable and generally expected to have higher solubility. The packing energy calculation for salts of isomeric ABA suggests that C-6 (E = –87.6 kJ mol^{-1}) is more stable than C-4 (E = –84.4 kJ mol^{-1}) by –3.2 kJ mol^{-1}, which supports the observed low aqueous solubility for C-6. The crystal structure of C-5 was obtained after removing the highly disordered water molecule of crystallization using the PLATON SQUEEZE program. Therefore, this parameter calculated for C-5 is not the real packing energy. To attain a homogeneous packing stability comparison among the rest of the crystal structures, the packing energy of C-5 is kept as the least stable structure.

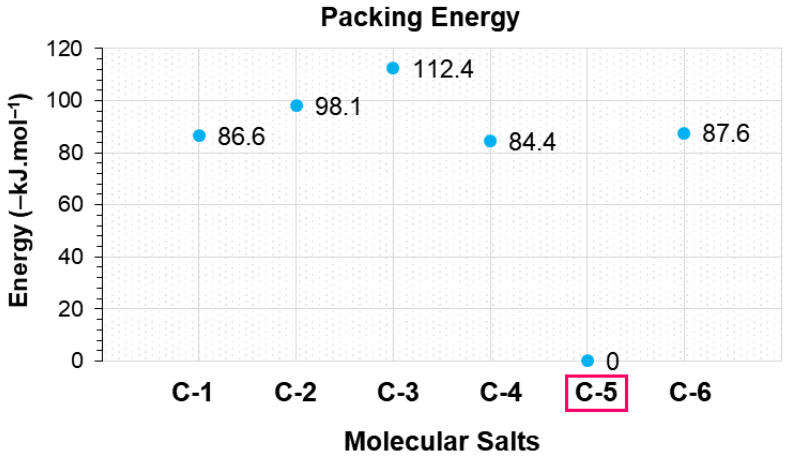

Figure 3.16 Relative packing energy comparison of molecular salts C-1 to C-6. The C-5 structure is obtained after removing highly disordered water molecule of crystallization using the PLATON SQUEEZE program. Thus, this parameter is not the actual packing energy for C-5. Perhaps, this value is kept as a reference to attain a homogeneous packing stability comparison among the rest of the crystal structures.

In the case of isomeric HBA salts, C-3 displays the highest packing energy (E = –112.4 kJ mol^{-1}) followed by C-2 (E = –98.1 kJ mol^{-1}) and C-1 (E = –86.6 kJ mol^{-1}) that indicates stability order of C-1 < C-2 < C-3. But the observed aqueous solubility order for the salts is C-2 > C-3 > C-1. Product C-1 displays the lowest solubility despite having the lowest packing energy. This may be due to the formation of a stronger hydrogen-bonded synthon in product C-1 as compared to C-2 and C-3. Among isomeric mono-HBA, the COOH group of *o*-HBA is the best proton donor with pK_a = 2.79. It forms a stronger and directional hydrogen-bonded supramolecular synthon (bond length (0.77 Å) and bond

angle (175°) with FAM as compared to *p*-HBA (0.78 Å and 170°, respectively) and *m*-HBA (0.88 Å and 164.0°, respectively) (Table 3.3). The relative synthon energy comparison is presented in Figure 3.17b. The synthon energy in C-1 (E = –11.06 kcal mol^{-1}) is seen to be higher than C-2 (E = –8.5 kcal mol^{-1}) and C-3 (E = –1.45 kcal·mol^{-1}) by –2.56 kcal mol^{-1} and –9.61 kcal mol^{-1} respectively. Moreover, the crystal structures reveal that salts with weaker synthon energy (C-2 and C-3) have one more free hydrogen bond acceptor site (–S=O) from the sulfonamide group, which may enable them to interact easily with the polar solvent and make them relatively more soluble than C-1.

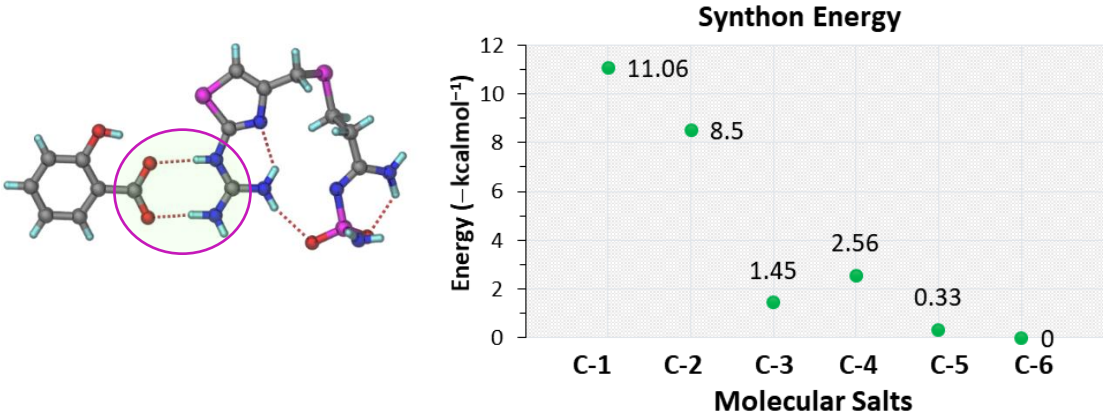

(a) (b)

Figure 3.17 (a) Main hydrogen-bonded synthon observed in all crystal structures from C-1 to C-6. (b) Relative energy values of the prime hydrogen-bonded synthon in the crystal structures of C-1 to C-6. The energy values were calculated using Gaussian09 on DFT with B3LYP; 6311G*(d, p) as the basic level.

3.3.6 Membrane Permeation Behaviour

In vitro permeation rate and drug flux of multicomponent solids of FAM were measured at pH 1.2 and 7.4 to examine the effects of change in a type and/or isomeric position of the functional group of coformer on a drug diffusion rate and flux (Figures 3.18 and 19). Marginal variation in the membrane permeation rate was observed among the new multicomponent solids of FAM. Products of *meta*-substituted coformers (C-2 and C-5) showed the fastest release rate among the products and the API (Figure 3.18a). A sharp rise in drug flux was observed for all of the products and pure API within 5 min (Figure 3.18b). All of the multicomponent solids demonstrated a higher drug flux than the parent drug during the lag time. Regardless of the functional groups on the coformers, salts from the same isomeric position coformers displayed approximately similar permeation behaviors. The similarity in the conformation of FAM in the crystal structures of these

salts can be one of the reasons behind this (Figure 3.11). Salts of *meta*-substituted coformers (C-2 and C-5) showed the highest drug flux, followed by salts of *ortho- and para*-substituted coformers (Figure 3.18b). A close observation of the crystal structure reveals that one O–H donor from the water molecules present in the crystal system is not involved in the hydrogen bonding formation with any acceptor in the structures of C-3 and

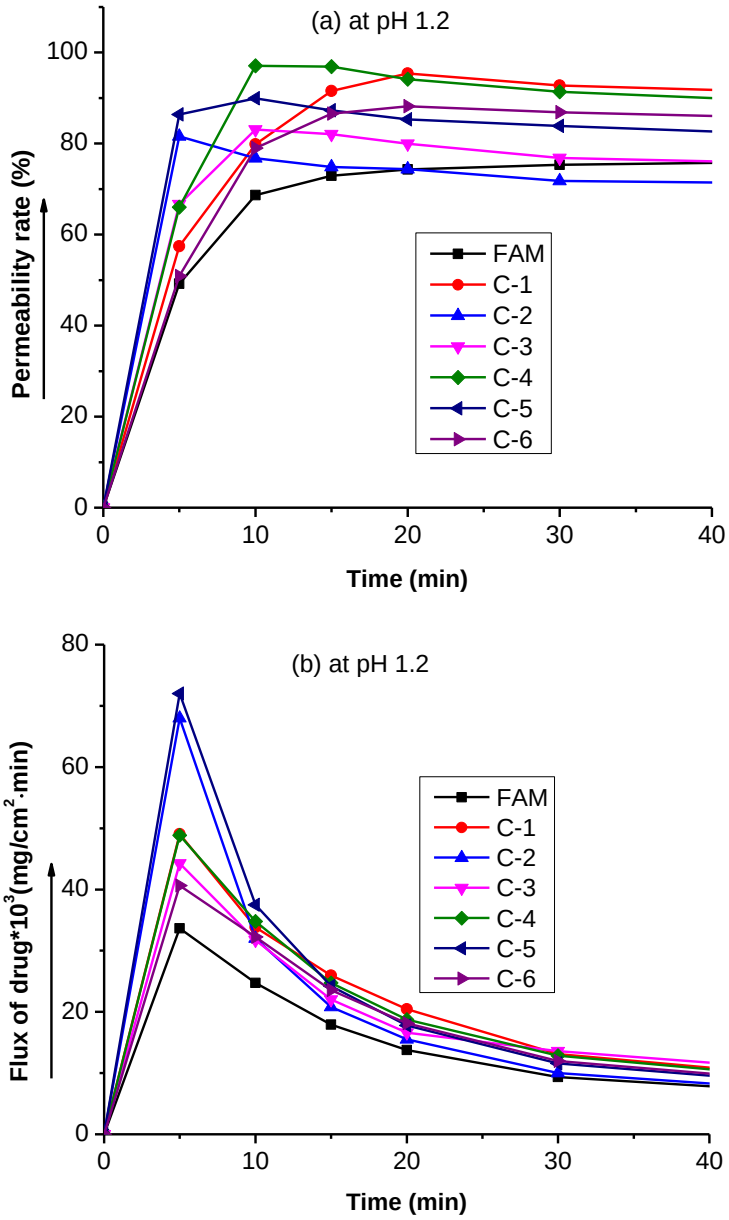

Figure 3.18 (a) Permeability rate percentage and (b) drug flux of FAM and its salts with time at pH 1.2.

C-6. This indicates that one of the hydrogen atoms of water molecules is free and available for weak noncovalent interactions with the polar solvent. Hence, it increases the polarity nature of these salts and reduces the membrane permeation of products C-3 and C-6. Moreover, the amino group of *p*-ABA in the structure of C-6 is free and available to

interact with the solvent medium. Thus, C-6 exhibits the lowest drug flux compared to all of the other salts. It can be observed from the plot of drug flux calculated at 180 min that the membrane permeation of all salt products is higher than that of the parent drug (Figure A4a, Appendix). Thus, all of the product materials exhibit better permeation properties than the parent drug molecule at pH 1.2.

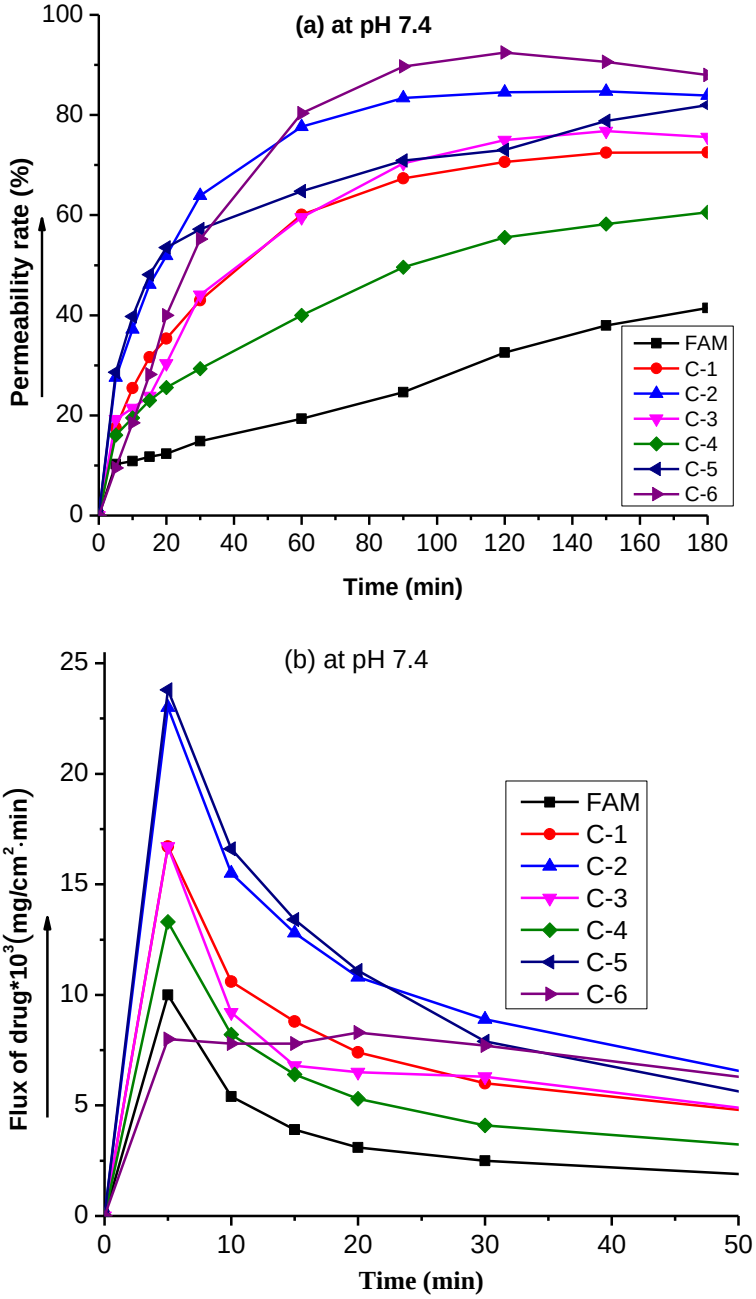

Figure 3.19 (a) Permeability rate percentage and (b) flux of FAM and its salts with time at pH 7.4.

The permeation rate for all products gradually increases with time at pH 7.4 (Figure 3.19a). The plot of drug flux shows that all products reached a sharp peak at 5 min and displayed

a higher amount of drug flux than API, except C-6**,** which showed a slight increase in drug flux in the steady-state region (Figure 3.19b). Salt products of *meta*-substituted coformers (C-2 and C-5) exhibit the highest amount of drug flux among the products during the lag time (Figures 3.19b). The final drug flux of the FAM and its salts calculated at 3 h demonstrates the multicomponent solids superiority over API at pH 7.4. Each product displayed a unique permeation behavior. Thus, salt formation of FAM with different isomeric HBA and ABA has resulted in not only multicomponent solids that differ in their membrane permeation but also improved the membrane permeability behavior of the drug. The quantity of drug flux at 3 h is 1.64 and 1.82 times that of the parent API for C-3 and C-6**,** respectively, 1.73 times that of the parent API for both C-2 and C-5, and 1.55 and 1.27 times that of the parent API for C-1 and C-4 products, respectively (Figure A4b, Appendix).

3.3.7 Hirshfeld Surface Analysis

Hirshfeld surface analysis was performed for the crystal structure of FAM and its salts using Crystal Explorer, version 21.5, to study the effect of drug-coformer intermolecular interactions on the solubility and permeability behaviors. The quantity of different noncovalent interactions that exist in the pure API and its salt forms is presented in the histogram (Figure 3.20). The PLATON SQUEEZED structure was used for product C-5 to analyze the contribution of each intermolecular interaction. Hence, the value presented for C-5 in the plot might be different from the actual one. It is apparent from the histogram that the main difference between the pure drug and its salt products is the contribution percentage of polar interactions (H···O, H···N, and H···S). However, the contribution percentage of the nonpolar interactions (H···C) has changed only slightly. The contribution of strong polar H···O interaction is higher in the products than that of pure API due to the presence of water and polar coformer molecules in their crystal lattices. In contrast, the percentage of relatively less polar H···N and H···S interactions significantly decreased after salt formation. The increase of polarity for the salt forms of the drug enhances the solute–solvent interactions, which is one of the possible reasons for the observed improvement of their aqueous solubility. But enhancing the drug polarity usually reduces its membrane permeation [40]. Product C-6 demonstrated lower drug flux because of the higher polar O–H interaction (33.9%), whereas C-5 showed higher drug flux in polar solvent as it has lower O–H interaction (24.3%). The drug diffusion rate through the membrane can also

be influenced by nonpolar interactions between the nonpolar moiety on the crystal surface of the drug and the cell membrane. Moreover, the nature of included coformer and the arrangement of molecules /ions in the crystal lattice may also take part in modulating the physicochemical property of drug molecules.

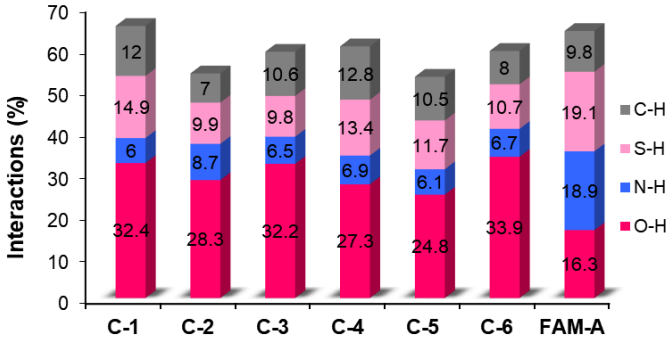

Figure 3.20 Percentage contribution of noncovalent interactions obtained using Hirshfeld surface area analysis of FAM and its salts C-1 to C-6.

3.4 Summary

Salt and/or cocrystal formation is a favored technique in pharmaceutical solid dose manufacturing plants for effective and safe dosage forms of numerous drugs, essentially those that come with inadequacy in physiochemical properties and stability. It provides superior concentration and stability than those of the parent nonionized forms of the drug. Six molecular salts of the easily degradable drug famotidine with isomeric hydroxybenzoic acids and isomeric aminobenzoic acids were synthesized. These molecular salts exhibited superior drug stability under different physiological environments. They further showed different but improved solubility and superior membrane permeability when compared with pure FAM. On a finer note, how such properties fluctuate with the change in the isomeric position and type of a functional group in the coformer was studied. Improved properties exhibited by these solid dosages are founded on the probability of forming stronger hydrogen-bonded heterosynthons present in the crystal structures, and this too fostered a significant conformational change in the drug molecule to protect from acid hydrolysis of the basic imine group in the amidine moiety.

3.5 Experimental Section

3.5.1 Materials

Famotidine (purity = 99%) was purchased from Yarrow chem Products and used as received. The marketed material was checked for polymorphic purity with respect to the

reported single crystal structures of the two polymorphs and found to be a mixture of both forms. All coformers were purchased from Sigma-Aldrich, India. HPLC-grade methanol used for crystallization was purchased from Merck, India. The solubility and permeability experiments were done by preparing buffer solutions of pH 1.2 and 7.4 using Millipore water.

3.5.2 Synthesis of Molecular Salt Hydrates

Famotidine salts were prepared using neat grinding and liquid-assisted mechanochemical grinding methods with a few drops of water. API and their respective coformers were mixed in a 1:1 stoichiometric ratio in the mortar and ground with a pestle for about 1 h with dropwise addition of water to prepare the organic salts. These ground materials were taken in a 25 mL conical flask and dissolved in methanol for crystallization. The solutions were kept undisturbed at ambient temperature for the slow evaporation of solvents. Suitable crystals were obtained for single crystal data collection after 2–4 days. The obtained products were characterized using FT-IR, DSC, TGA, PXRD, and single crystal X-RD techniques.

3.5.3 Vibrational Spectroscopy (FT-IR)

Before recording the IR spectra, a small quantity of the sample was ground with 1% KBr. A PerkinElmer Frontier MIR FT-IR spectrophotometer was used to record the IR spectra of the samples. The significant stretching of IR spectra (cm^{-1}) for FAM and the obtained products, FAM: 3508, 3401 (N–H), 1145 (S=O), 1644, 1603 (C=N); **C-1**: 3497 (O–H), 3371-3228 (N–H), 1137(S=O), 1573 & 1378 (COO^-), 1628 (C=N); **C-2**: 3485 (O–H), 3415-3337 (N–H), 1126 (S=O), 1570 & 1384 (COO^-), 1629 (C=N); **C-3**: 3527 (O–H), 3385-3354 (N–H), 1131(S=O), 1575 & 1373 (COO^-), 1629 (C=N); **C-4**: 3535 (O–H), 3474-3374 (N–H), 1136(S=O), 1575 & 1380 (COO^-), 1611 (C=N); **C-5**: 3606 (O–H), 3437-3332 (N–H), 1138(S=O), 1547 & 1385 (COO^-), 1629 (C=N); **C-5**: 3576 (O–H), 3461-3367 (N–H), 1130(S=O), 1576 & 1378 (COO^-), 1628 (C=N).

3.5.4 Differential Scanning Calorimetry (DSC)

A Shimadzu DSC 60 model was used to record the DSC thermograms of all of the samples. A sample amount of 4–5 mg was transferred to a pan and sealed with an aluminum plate. Then, the sample pan was heated in a temperature range of 25–300 °C at a rate of 25 °C/min under a continuous flow of dry nitrogen at a rate of 30 mL/min. The observed

melting temperatures of all six products are compared with those of the starting materials and presented in Table 3.4. Before recording, calibration of the instrument was done to ensure the accuracy of heat flow and temperature using the melting of pure indium.

3.5.5 Thermogravimetric Analysis (TGA)

The TGA of the samples was recorded using the Mettler Toledo TGA/SDTA 851e module to determine the amount of solvent present in the product materials. A sample amount of 3–5 mg was taken in an alumina pan and heated in the temperature range of 30–300 °C at a rate of 10 °C/min under a dry nitrogen flow of 30 mL/min.

3.5.6 Powder X-ray Diffraction (PXRD)

The PXRD of all of the products was recorded on a Bruker D8 Focus X-ray diffractometer, Germany. The data recording was carried out using anode material of Cu Kα X-radiation (λ = l.54056 Å) at 35 kV and 25 mA at a scan rate of 1 °min^{-1} within the 2θ range 10–50°. Rietveld refinement using Powder Cell 2.3 was done to check the phase purity and homogeneity of the product materials (Figure A2, Appendix).

3.5.7 Single Crystal X-ray Diffraction (Single Crystal X-RD)

Single crystal X-RD data was collected on a Bruker APEX-II CCD diffractometer using the radiation of Mo Kα (λ = 0.71073 Å). Water molecule was removed from C-5 using the PLATON SQUEEZE program to eliminate the solvent disorder. The details of the crystallographic data of all of the crystals are presented in Appendix Table A2. Hydrogen bond parameters are listed in Table 3.5 and neutron-normalized to fix the D–H distance to its accurate neutron value of O–H 0.983 Å, N–H 1.009 Å, and C–H 1.083 Å.

3.5.8 Cambridge Structural Database (CSD)

The CSD survey was carried out with the latest version, CSD 2022.1 software coupled with Mercury 4.1.0. An overlay of FAM conformers extracted from the crystal structures of the molecular salts was drawn on Mercury 4.1 (Figure 3.11).

3.5.9 DFT Calculation

The energy values of the hydrogen-bonded synthons in the crystal structure of the molecular salt were calculated using Gaussian09 on DFT with B3LYP; 6311G *(d, p) as the basic level (Figure 3.17b).

3.5.10 Hirshfeld Surface Analysis

The contribution percentage of various intermolecular interactions of salt hydrates was calculated using Crystal Explorer version 21 at the B3LYP/6-31G *(d, p) level of theory (Figures 3.20).

3.5.11 Phase Stability

A slurry of each product material was prepared to test its stability in an aqueous medium and at pH 1.2 and 7.4. The product material was added to 2–3 mL of solutions and stirred for 24 h at room temperature. Some portion of the sample was retrieved from the slurry at time intervals of 1, 12, 20, and 24 h. The samples were allowed to dry for a while, and their PXRD patterns were recorded and compared with simulated patterns.

3.5.12 Solubility Study

Using UV–visible spectroscopy, the solubility of pure FAM and its salts was determined in an aqueous medium and at pH 1.2 and 7.4. The experiment was done following the reported procedures in the literature [41–44]. All experiments were measured on a Shimadzu UV-2550 UV–visible double-beam spectrophotometer. An excess amount of FAM and each product material was added in 5 mL of water or buffer solutions (pH 1.2 and 7.4) and then stirred at 800 rpm for 24 h at the ambient temperature of 28 °C. The solution was filtered using Whatman filter paper 1 with a pore size of 11 μm, and then absorbance of the solutions was obtained by measuring ultraviolet (UV) absorption. The concentration of an unknown solution (C_u) of the salts was obtained from the slope and the intercept of the calibration curve using the formula $C_u = (A_u – \text{intercept})/\text{slope}$, where A_u is the absorbance of the unknown solution.

3.5.13 Membrane Permeability Study

A membrane permeability study of FAM and its product materials was performed using a dialysis membrane-135 purchased from HiMedia, India, in a diffusion apparatus. All of the experiments were carried out according to the reported procedures in the literature [42,43]. The dialysis membrane-135 had an average flat width of 39.41 mm, a diameter of 23.8 mm, and a capacity of ~4.45 mL/cm. The sample (5 mg) was prepared in the dialysis membrane as a donor compartment and placed in the receptor compartment containing 100 mL of buffer solutions of pH 1.2 or 7.4. The sample solution was then stirred at 800 rpm at room temperature (28 °C) and allowed to diffuse via the membrane toward the receptor

compartment. Four milliliters of the sample were taken from the receptor compartment at a definite time interval. To keep the volume of the solution constant, exactly 4 mL of the fresh solution was added to the receptor compartment each time. The quantity of sample released toward the receptor compartment via the dialysis membrane was measured using UV–visible spectrophotometry for each predetermined time interval.

3.6 References

[1] Steed, J. W. The role of co-crystals in pharmaceutical design. *Trends in pharmacological sciences*, 34(3):185-193, 2013.

[2] Saikia, B., Pathak, D., and Sarma, B. Variable stoichiometry cocrystals: occurrence and significance. *CrystEngComm*, 23(26):4583-4606, 2021.

[3] Duggirala, N. K., Perry, M. L., Almarsson, Ö., and Zaworotko, M. J. Pharmaceutical cocrystals: along the path to improved medicines. *Chemical Communications*, 52(4):640-655, 2016.

[4] Nangia, A. K. and Desiraju, G. R. Crystal Engineering: An Outlook for the Future. *Angewandte Chemie International Edition*, 58(13):4100-4107, 2019.

[5] Bolla, G., Sarma, B., and Nangia, A. K. Crystal engineering and pharmaceutical crystallization. In: *Hot Topics in Crystal Engineering*. Elsevier; 2021:157-229.

[6] Khatioda, R., Bora, P., and Sarma, B. Trimorphic ethenzamide cocrystal: in vitro solubility and membrane efflux studies. *Crystal Growth & Design*, 18(8):4637-4645, 2018.

[7] Amidon, G. L., Lennernäs, H., Shah, V. P., and Crison, J. R. A theoretical basis for a biopharmaceutic drug classification: the correlation of in vitro drug product dissolution and in vivo bioavailability. *Pharmaceutical research*, 12(3):413-420, 1995.

[8] Bighley, L. D., Berge, S. M., and Monkhouse, D. C. Salt forms of drugs and absorption. *Encyclopedia of Pharmaceutical Technology*, 13:453-499, 1996.

[9] Gu, C. H., Grant, D. J. W., Eichelbaum, M., Testa, B., and Somogyi, A. *Handbook of Experimental Pharmacology: Stereochemical Aspects of Drug Action and Disposition*.; 2003.

[10] Stahl, P. H. and Wermuth, C. G. Handbook of pharmaceutical salts: properties, selection and use. *Chem. Int*, 24:21, 2002.

[11] Serajuddin, A. T. M. Salt formation to improve drug solubility. *Advanced drug delivery reviews*, 59(7):603-616, 2007.

[12] Sarma, B., Thakuria, R., Nath, N. K., and Nangia, A. Crystal structures of mirtazapine molecular salts. *CrystEngComm*, 13(9):3232-3240, 2011.

[13] Schultheiss, N., and Newman, A. Pharmaceutical Cocrystals and Their Physicochemical Properties. *Crystal Growth & Design*, 9(6):2950-2967, 2009.

[14] Li, D., Li, J., Deng, Z., and Zhang, H. Piroxicam–clonixin drug–drug cocrystal solvates with enhanced hydration stability. *CrystEngComm*, 21(28):4145-4149, 2019.

[15] Karimi-Jafari, M., Padrela, L., Walker, G. M., and Croker, D. M. Creating cocrystals: A review of pharmaceutical cocrystal preparation routes and applications. *Crystal Growth & Design*, 18(10):6370-6387, 2018.

[16] Baldrighi, M., Cavallo, G., Chierotti, M. R., Gobetto, R., Metrangolo, P., Pilati, T., Resnati, G., and Terraneo, G. Halogen Bonding and Pharmaceutical Cocrystals: The Case of a Widely Used Preservative. *Molecular Pharmaceutics*, 10(5):1760-1772, 2013.

[17] Ketkar, S., Pagire, S. K., Goud, N. R., Mahadik, K., Nangia, A., and Paradkar, A. Tracing the architecture of caffeic acid phenethyl ester cocrystals: studies on crystal structure, solubility, and bioavailability implications. *Crystal Growth & Design*, 16(10):5710-5716, 2016.

[18] Aitipamula, S., Chow, P. S., and Tan, R. B. H. Trimorphs of a pharmaceutical cocrystal involving two active pharmaceutical ingredients: potential relevance to combination drugs. *CrystEngComm*, 11(9):1823-1827, 2009.

[19] Thakuria, R. and Sarma, B. Drug-drug and drug-nutraceutical cocrystal/salt as alternative medicine for combination therapy: a crystal engineering approach. *Crystals*, 8(2):101, 2018.

[20] Saikia, B., Sultana, N., Kaushik, T., and Sarma, B. Engineering a Remedy to Improve Phase Stability of Famotidine under Physiological pH Environments. *Crystal Growth and Design*, 19(11):6472-6481, 2019.

[21] Langtry, H. D., Grant, S. M., and Goa, K. L. Famotidine. *Drugs*, 38(4):551-590, 1989.

[22] Suleiman, M. S., Najib, N. M., Hassan, M. A., and Abdel-Hamid, M. E. Kinetics of the acid-catalyzed hydrolysis of famotidine. *International Journal of Pharmaceutics*, 54(1):65-69, 1989.

[23] Melo, S. R. de O., Homem-de-Mello, M., Silveira, D., and Simeoni, L. A. Advice on Degradation Products in Pharmaceuticals: A Toxicological Evaluation. *PDA*

Journal of Pharmaceutical Science and Technology, 68(3):221-238, 2014.

[24] Cheng, W.-T. and Lin, S.-Y. Famotidine polymorphic transformation in the grinding process significantly depends on environmental humidity or water content. *International Journal of Pharmaceutics*, 357(1):164-168, 2008.

[25] Mady, F. M., Abou-Taleb, A. E., Khaled, K. A., Yamasaki, K., Iohara, D., Taguchi, K., Anraku, M., Hirayama, F., Uekama, K., and Otagiri, M. Evaluation of carboxymethyl-β-cyclodextrin with acid function: Improvement of chemical stability, oral bioavailability and bitter taste of famotidine. *International Journal of Pharmaceutics*, 397(1):1-8, 2010.

[26] Yuliandra, Y., Fitriani, L., Kurniawan, R., Yasardi, F., and Zaini, E. Solid Dispersions of Famotidine: Physicochemical Properties and In Vivo Comparative Study on the Inhibition of Hyperacidity. *ChemistrySelect*, 5(29):9218-9225, 2020.

[27] Brittain, H. G. Active Pharmaceutical Ingredient DRUG DEVELOPMENT: Developing an Appropriate Salt Form for an Center for Pharmaceutical Physics. *American Pharmaceutical Review*, 12(7):62, 2009.

[28] Russo, M. G., Brusau, E. V, Ellena, J., and Narda, G. E. Solid-State Supramolecular Synthesis Based on the N–H…O Heterosynthon: An Approach to Solve the Polymorphism Problem in Famotidine. *Journal of Pharmaceutical Sciences*, 103(11):3754-3763, 2014.

[29] Zhang, Y., Yang, Z., Zhang, S., and Zhou, X. Synthesis, crystal structure, and solubility analysis of a famotidine cocrystal. *Crystals*, 9(7):3-12, 2019.

[30] Marosi, A., Szalay, Z., Béni, S., Szakács, Z., Gáti, T., Rácz, Á., Noszál, B., and Demeter, Á. Solution-state NMR spectroscopy of famotidine revisited: spectral assignment, protonation sites, and their structural consequences. *Analytical and Bioanalytical Chemistry*, 402(4):1653-1666, 2012.

[31] Childs, S. L., Stahly, G. P., and Park, A. The Salt−Cocrystal Continuum: The Influence of Crystal Structure on Ionization State. *Molecular Pharmaceutics*, 4(3):323-338, 2007.

[32] Sarma, B., Nath, N. K., Bhogala, B. R., and Nangia, A. Synthon Competition and Cooperation in Molecular Salts of Hydroxybenzoic Acids and Aminopyridines. *Crystal Growth & Design*, 9(3):1546-1557, 2009.

[33] Bolla, G. and Nangia, A. Clofazimine Mesylate: A High Solubility Stable Salt. *Crystal Growth & Design*, 12(12):6250-6259, 2012.

[34] Cruz-Cabeza, A. J. Acid–base crystalline complexes and the pKa rule.

CrystEngComm, 14(20):6362-6365, 2012.

[35] Tothadi, S., Shaikh, T. R., Gupta, S., Dandela, R., Vinod, C. P., and Nangia, A. K. Can We Identify the Salt–Cocrystal Continuum State Using XPS? *Crystal Growth & Design*, 21(2):735-747, 2021.

[36] Babu, N. J., Sanphui, P., and Nangia, A. Crystal Engineering of Stable Temozolomide Cocrystals. *Chemistry – An Asian Journal*, 7(10):2274-2285, 2012.

[37] Trask, A. V, Motherwell, W. D. S., and Jones, W. Pharmaceutical cocrystallization: engineering a remedy for caffeine hydration. *Crystal Growth & Design*, 5(3):1013-1021, 2005.

[38] Wang, J.-R., Zhou, C., Yu, X., and Mei, X. Stabilizing vitamin D3 by conformationally selective co-crystallization. *Chemical Communications*, 50(7):855-858, 2014.

[39] Yu, Q., Yan, Z., Bao, J., Wang, J.-R., and Mei, X. Taming photo-induced oxidation degradation of dihydropyridine drugs through cocrystallization. *Chemical Communications*, 53(91):12266-12269, 2017.

[40] Sanphui, P., Devi, V. K., Clara, D., Malviya, N., Ganguly, S., and Desiraju, G. R. Cocrystals of Hydrochlorothiazide: Solubility and Diffusion/Permeability Enhancements through Drug–Coformer Interactions. *Molecular Pharmaceutics*, 12(5):1615-1622, 2015.

[41] Sarma, B. and Saikia, B. Hydrogen bond synthon competition in the stabilization of theophylline cocrystals. *CrystEngComm*, 16(22):4753-4765, 2014.

[42] Bommaka, M. K., Chaitanya Mannava, M. K., Suresh, K., Gunnam, A., and Nangia, A. Entacapone: Improving aqueous solubility, diffusion permeability, and cocrystal stability with theophylline. *Crystal Growth and Design*, 18(10):6061-6069, 2018.

[43] Bora, P., Saikia, B., and Sarma, B. Regulation of π···π Stacking Interactions in Small Molecule Cocrystals and/or Salts for Physiochemical Property Modulation. *Crystal Growth & Design*, 18(3):1448-1458, 2018.

[44] Saikia, B., Bora, P., Khatioda, R., and Sarma, B. Hydrogen Bond Synthons in the Interplay of Solubility and Membrane Permeability/Diffusion in Variable Stoichiometry Drug Cocrystals. *Crystal Growth and Design*, 15(11):5593-5603, 2015.